60-GHz Millimeter-Wave Propagation Inside Bus: Measurement, Modeling, Simulation, and Performance Analysis

ANIRUDDHA CHANDRA[1], (Senior Member, IEEE), ANIQ UR RAHMAN[1], (Student Member, IEEE), USHASI GHOSH[1], (Student Member, IEEE), JOSÉ A. GARCÍA-NAYA[2], (Member, IEEE), ALEŠ PROKEŠ[3], JIRI BLUMENSTEIN[3], (Member, IEEE), AND CHRISTOPH F. MECKLENBRÄUKER[4], (Senior Member, IEEE)

[1]Department of Electronics and Communication Engineering, National Institute of Technology, Durgapur 713209, India
[2]CITIC Research Center, Universidade da Coruña, 15071 A Coruña, Spain
[3]Department of Radio Electronics, Brno University of Technology, 61200 Brno, Czech Republic
[4]Christian Doppler Laboratory, Institute of Telecommunications, Vienna University of Technology, 1030 Vienna, Austria

Corresponding author: Aleš Prokeš (prokes@feec.vutbr.cz)

ABSTRACT Millimeter-wave (mmWave) transmission over the unlicensed 60-GHz spectrum is a potential solution to realize high-speed internet access, even inside mass transit vehicles. The solution involves communication between users and a mmWave-band on-board unit that aggregates/disseminates data streams from/to commuters and maintains the connection with the nearest terrestrial network infrastructure node. In this paper, we provide a measurement-based channel model for the 60-GHz mmWave propagation inside a typical inter-city bus. The model characterizes power delay profile (PDP) of the wireless intra-vehicular channel, and it is derived from about 1000 data sets measured within the bus. The proposed analytical model is further translated into a simple simulation algorithm that generates in-vehicle channel PDPs. Different goodness-of-fit tests confirm that the simulated PDPs are in good agreement with the measured data. Finally, a tapped-delay-line (TDL) channel model is formulated from the proposed PDP model, and the TDL model is used to study the bit error rate (BER) performance of the mmWave link inside bus under varying data rates and link lengths.

INDEX TERMS Intra-vehicular communication, 60 GHz channel sounding, power delay profile, tapped delay line, bit error rate.

I. INTRODUCTION

Remaining connected while on-the-move is the mantra of the next generation commuters [1]. Over the last two decades, there had been a steady increase in long distance commuting as a result of urbanization of employment opportunities [2]. According to the European Union (EU) labor force survey conducted in 2015, 8% of the EU workforce commuted to

work in a different region, and 1% commuted cross-border. The average commute time per day is about 1.1 hours [3], with around 10% extreme commuters spending more than 2 hours per day [4]. Driving personal cars for commuting is a unproductive task and leads to unnecessary stress. By letting someone else to do the driving, connected commuters can utilize the unpaid time for working, gathering information, or enjoying multimedia streaming [5].

For a daily commuter, public transport vehicles (e.g., buses, trains, and ferries) are cost-effective and
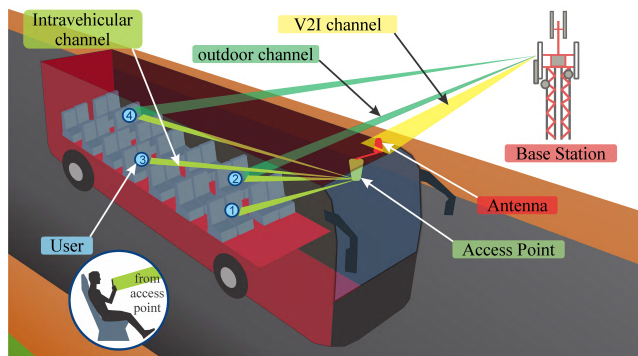
The associate editor coordinating the review of this manuscript and approving it for publication was Ke Guan.

FIGURE 1. Network access during commute.

environmentally friendly alternatives, providing easy access to major urban joints and alleviating the user from parking worries. On top of that, policymakers are working hard to achieve car-free cities [6], [7] through subsidies and awareness campaigns. In spite of these, the shift in the commuting mode is sluggish [8]–[10] and the transportation sector is in desperate need of a game changer. A large section of stakeholders believe that equipping public vehicles with on-board gigabit wireless networks can accelerate the shift considerably. The idea is illustrated in Fig. 1, where the access network forms a two-hop system: base stations (BSs) or road side units (RSUs) serve the vehicular access point (AP) over vehicle-to-infrastructure (V2I) mobile channels, and the vehicular AP connects to the passengers inside over static intravehicular channels.[1] The network architecture helps in avoiding the penetration loss caused by metallic bodies and signaling overhead due to group handovers [1] experienced in direct outdoor channels. There are many other potential applications of intravehicular wireless signaling beyond user connectivity, which include counting the number of passengers in a public vehicle [11] or establishing a small-scale social networking platform between co-passengers [12]. However, wireless communication infrastructures inside public vehicles should be able to provide such on-demand real-time high-data-rate diverse services.

Millimetre wave (mmWave) is a promising new technology [13] which is able to provide an enormous bandwidth to support the aforementioned diverse services in current fifth generation (5G) [14] and beyond 5G [15] networks. There had been already several initiatives to implement mmWave in intelligent transportation systems [16], [17]. In the 60 GHz unlicensed band, mmWave networks can provide up to 100 Gbit/s [18] in short-range limited-mobility scenarios, i.e., inside offices and buildings [19]–[21], or in specialized environments such as inside vehicles.

In general, mmWave propagation is significantly distinct when compared to narrowband sub-6 GHz propagation in several respects [22]: sparse multipath, high path-loss, directional transmission, lesser penetration, diffuse scattering, etc. In a closed space environment such as interior of a vehicle, the effect of some of these characteristics is magnified. Thus, experimental study of intravehicle mmWave propagation channel is of fundamental interest.

The 60 GHz mmWave propagation was earlier investigated for links between cars [23]–[25], for links inside cars [26]–[29], and for links inside aircrafts [30], [31]. Recent works also compare the 60 GHz mmWave transmission to the traditional ultra-wideband (UWB) transmission in the 3-11 GHz band [32]–[34]. However, mmWave channel models inside public transport vehicles such as buses have rarely been studied in depth. Previous works include narrowband measurements at 2.4 GHz [35], at 5 GHz [36], [37], and UWB measurements in the range of 2.3-11 GHz [38]. The only exceptions are [39] or authors' own works such as [40] and [41], in which some initial measurement data and preliminary channel modeling is presented for 60 GHz mmWave signal propagation inside a bus.

The electronic communications committee (ECC) recommendation on using 57-64 GHz band in 2009 [42] paved the way for 60 GHz mmWave-based pan-European cross-border experiments on connected and automated driving [43]. Standardization and regulation of such EU cooperative intelligent transport systems (C-ITSs) [44] is driven by car-2-car communication consortium (C2C-CC), European telecommunications standards institute (ETSI) and European committee for standardization (CEN). In this regard, the present work is the outcome of the collaboration between research groups in three different countries, namely Czech Republic, Austria, and Spain, in which we focus on intravehicular communications. The main contributions of this paper are detailed below.

- We provide measurement data for 60 GHz frequency-domain channel sounding inside a bus. Around a thousand data points have been recorded during the field trials. Instead of using a vector network analyzer (VNA) (which has range limitations due to the cable costs), we employed a signal analyzer, enabling us to cover the whole bus length.
- Unlike a VNA, a signal analyzer used as a receiver does not record the phase information. Instead, only the magnitude of the input signal for a defined frequency range is measured. Since the phase information is critical for a subsequent time-domain analysis, we propose a post-processing technique based on the Hilbert transform to reproduce the phase of the channel transfer function (CTF) from the recorded signal amplitude and the transmitter-receiver distance (d) measured in the 3D space. The data from a previous measurement campaign [29], in which a passenger car was considered, is employed to validate the accuracy of the proposed technique.

---

[1]The outdoor channel referred in Fig. 1 is basically an outdoor-to-indoor channel penetrating the vehicle and is used by a commuter to directly connect with a BS or RSU when there is no provision of connecting to an in-vehicle AP. Further, the AP needs to be equipped with two antennas, one outside the vehicle, which connects to the nearest BS/ RSU and has a wired connection to the AP fitted inside the vehicle, and another inside the vehicle attached to the AP, which connects to the user devices.
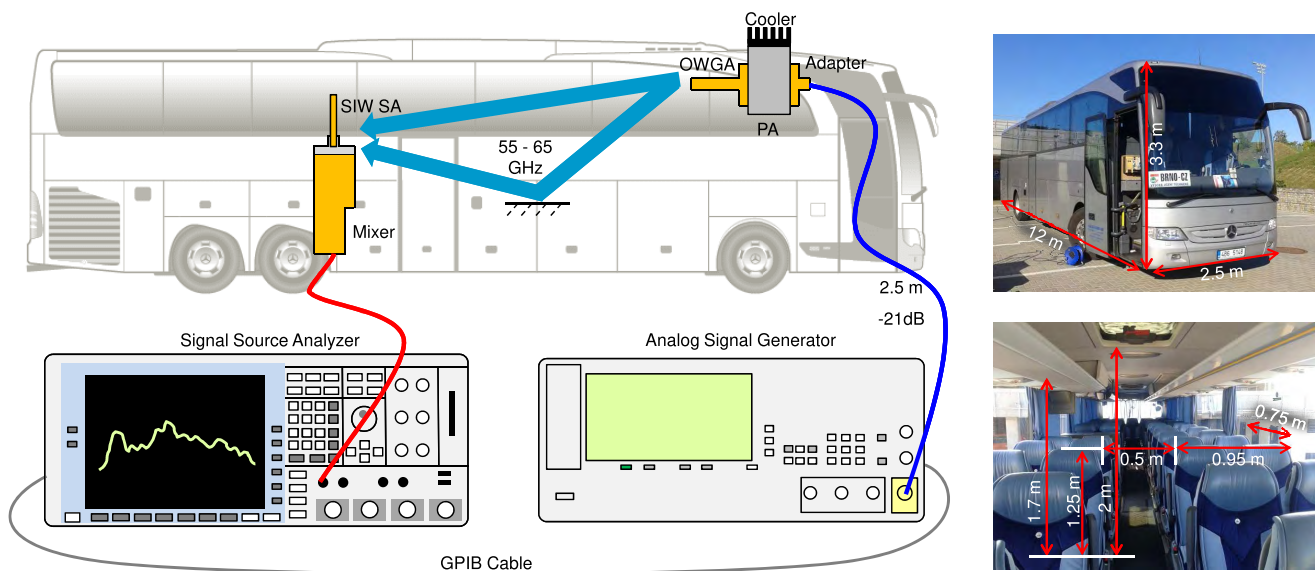
FIGURE 2. Measurement setup [left]. The bus from outside [right-top] and inside [right-bottom].

- Power delay profiles (PDPs) are obtained from the frequency-domain sounding data by means of the complex-valued inverse fast Fourier transform (IFFT). General PDP trends are identified, which helped to perform an analytical characterization and subsequently led to a simple PDP simulation algorithm which requires only the receiver-transmitter distance d as an input. Additionally, the performance of the algorithm has been evaluated and validated with several goodness-of-fit (GoF) tests.

- Discrete-time PDPs are derived from the continuous-time PDPs, hence the channel can be modeled as a tapped-delay-line (TDL) filter for link-level simulations. The entire simulation code along with the recorded data set is made available through IEEE Code Ocean platform (DOI: 10.24433/CO.1876676.v1). The TDL model is used to study the bit error rate (BER) performance of the mmWave link inside the bus with varying data rates and link lengths.

The rest of the paper is organized as follows. In Section II, we discuss the experimental setup employed for the channel measurements. The post processing method using the Hilbert transform is presented in Section III. In Section IV, we discuss our analytical PDP model and introduce the PDP simulation algorithm. Section V presents of the TDL model and the results of the BER simulations. Finally, Section VI concludes the paper.

II. FIELD EXPERIMENTS

Field experiments were performed at Brno University of Technology campus in Czech Republic. The vehicle used is a 50-seater long-distance inter-city coach (model: Mercedes Benz Tourismo BlueTec4), parked in front of a covered garage. There were no other cars on the parking lot during measurements and the immediate surroundings have no buildings or concrete structures. The bus has a dimension of 12 m (length) by 2.5 m (width) by 3.3 m (height). Inside, the floor-to-ceiling distance is 2 m, the overhead luggage rack is at 1.7 m height and each seat is 1.25 m high. The half-rows are 0.95 m wide on each side with an aisle space of 0.5 m in-between, and the distance between successive seat rows is 0.75 m. The exterior and interior of the bus is shown in Fig. 2.

The equipment used for the 60 GHz channel sounding inside the bus is also shown in Fig. 2. Channel sounding in the 60 GHz range is a non-trivial task: for the sub-40 GHz testing, 2.92 mm radio-frequency (RF) cables, connectors and off-the-shelf antennas are readily available, whereas for 60 GHz channel sounding, expensive 1.85 mm RF cables are needed and antennas have a waveguide coupling that requires waveguide to 1.85 mm cable adapters. Our measurements are performed in the frequency domain, with an experimental setup consisting of an analog signal generator (model: Agilent E8257D), a scalar signal analyzer (model: Rhode and Schwarz FSUP50), custom-built 60 GHz mmWave antennas, a power amplifier (PA) (model: Quinstar QPW 50662330) at the transmitter (Tx) end, a mixer (model: Rohde & Schwarz FS Z75) at the receiver (Rx) end, adapters, phase-stable coaxial cables (model: MegaPhase TM67), and a DC power supply (model: Diametral P230R51D). The generator output is set to 13 dBm, the PA has a gain of 31 dB and the resolution bandwidth of the analyzer is set to 10 kHz. The major advantage of the current setup over a VNA based setup is that the Tx and the Rx are connected to different hardware equipment. A general purpose interface bus (GPIB) cable connects the Tx and the Rx for synchronization, allowing for cascading two or more GPIB cables to extend the Tx-Rx distance. In contrast, for sounding with a VNA, both the Tx and the Rx must be
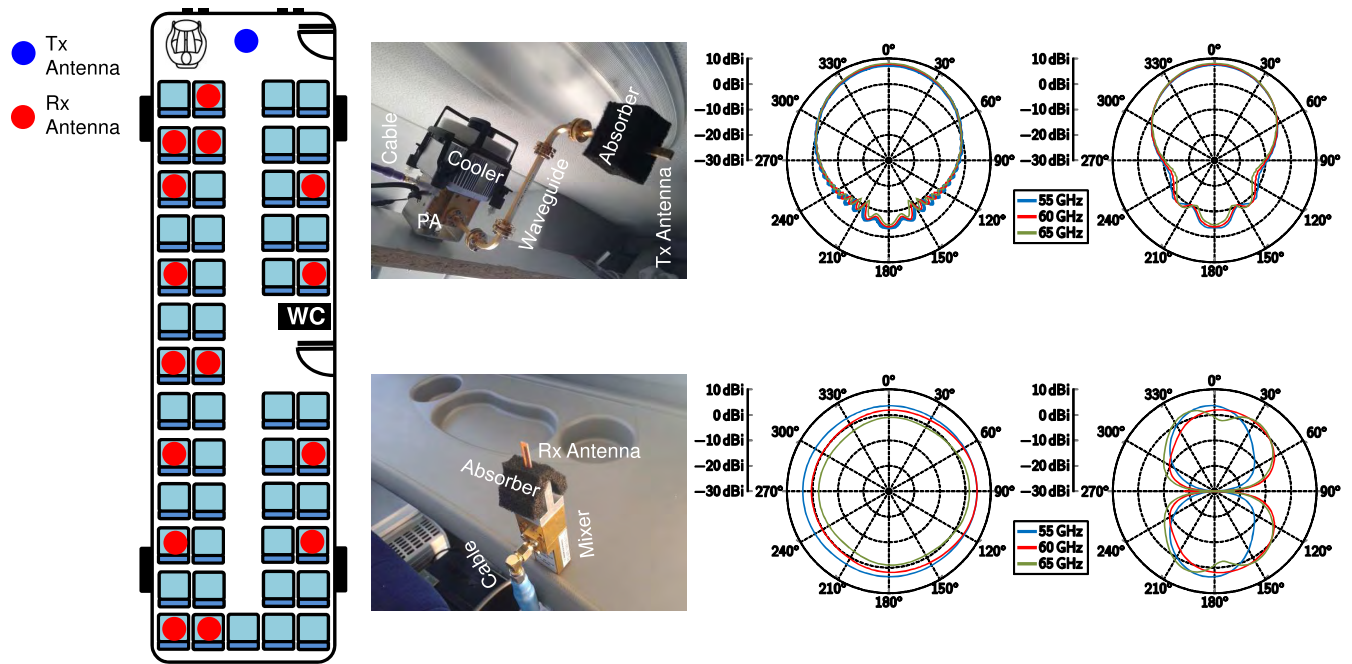
FIGURE 3. Placement of the antennas inside the bus [left], photographs of the antenna assemblies [middle], and simulated radiation patterns of the antennas both in the E-plane and in the H-plane [right].

connected to the VNA, facing large cable losses and thus limiting the Tx-Rx distance.

A bandwidth (BW) of 10 GHz was covered, ranging from 55GHz to 65 GHz and 60 GHz being the center frequency. 1001 measurement points were recorded in each sweep. A complete sweep requires 4 minutes. The CTF amplitude, $|H(f)|$, is recorded for each frequency point (f_i; $f_{i+1} - f_i = 10$ MHz). The output of the signal generator is sent, by means of a cable, to the PA, which is powered by the DC power supply and exhibits a gain to compensate for the cable losses and also to boost the signal to be fed to the open waveguide type Tx antenna (OWGA). At the receiver end, the signal is captured by a substrate-integrated-waveguide slot antenna (SIW SA) and is sent to the signal analyzer. Given that the signal analyzer can only work up to 50 GHz, an external mixer down-converts the signal to an intermediate frequency (IF) of 404.4 MHz, mitigating also the high cable losses at mmWave frequencies.

The position of the Tx and the Rx antennas inside the bus is shown in Fig. 3. Since our goal is to evaluate the performance of the 60 GHz downlink channel, the Rx antenna is attached to a drop-down seat tray, imitating the typical position of a handheld personal wireless device. To cover the entire space inside the bus, the Rx antenna was placed at 15 different seats during the course of the measurements. On the other hand, the position of the Tx antenna is placed near the ceiling and the bust front window to emulate a rooftop access point. The close-up of the antenna fixtures is also shown in Fig. 3. The absorbers are used to limit reflections from metal parts of the fixtures. There are a number of WR 15 type waveguides used between the PA

and the Tx antenna to point the antenna towards the desired direction.

As shown in Fig. 3, the radiation pattern of the Rx antenna is omni-directional (mobile user), whereas the Tx antenna (access point) is a directional waveguide, whose main beam is directed towards the seats to maximize directivity.

III. POST PROCESSING

Measurement setups based on VNAs are favored to carry out frequency-domain static wireless channel measurements/ sounding due to their robustness and high dynamic range. In spite of a static channel environment inside a bus, a VNA-based setup could not be employed for the channel measurements because the measurement distance would then have been restricted by the length of the coaxial cables. Contrarily, a signal analyzer cannot measure directly the phase of the captured signals, but the phase can be retrieved from the amplitude only measurement data to produce the complex-valued CTF. The complex-valued IFFT can then be applied to procure the channel response in the time domain.

Using the Hilbert Transform (HT), it is feasible to recover the phase information from the magnitude measurements of the received signal. One of the initial studies in this domain has been recorded in [45]. It considers two Hilbert-based techniques to derive the channel impulse response (CIR) in the sub-6 GHz frequency band, hence establishing the employability of a Hilbert-based estimation approach to recover phase information from amplitude only data. Similar HT-based techniques applied at higher frequencies have been presented in [46] and [47], but requiring that the CTF, $H(f)$, be a minimum phase function. The basic idea presented in

those papers can be demonstrated in the following manner. The complex-valued CTF in the frequency-domain can be written in polar form as

$$H(j\omega) = |H(j\omega)| \exp(j \arg[H(j\omega)]), \qquad (1)$$

and taking logarithms on both sides we have

$$\tilde{H}(j\omega) = \log_e\{|H(j\omega)|\} + j \arg[H(j\omega)], \qquad (2)$$

where $\log_e\{H(j\omega)\} = \log_e\{|H(j\omega)|\} + j \arg[H(j\omega)]$. Defining $\tilde{h}(n) = \mathcal{F}^{-1}[\tilde{H}(j\omega)]$ as the Fourier inverse of $\tilde{H}(j\omega)$, then the phase information can be obtained from the amplitude response [45] as follows

$$\arg[H(j\omega)] = \mathcal{H}[\log_e\{|H(j\omega)|\}], \qquad (3)$$

where $\mathcal{H}[\cdot]$ denotes the Hilbert transform assuming that $\tilde{h}(n)$ is causal, i.e., $\tilde{h}(n) = 0; \ n < 0$.

A. PROPOSED METHOD

In this subsection, we present our HT based approach to recover the phase information. The CTF need not be a minimum phase function in this case. However, it must be a causal function, a significantly weaker condition inflicted on the channel response.

The objective is to project the amplitude data into the real-valued component of the regenerated CTF employing the HT. Consequently, the phase delay is first derived as a function of the frequency. The phase difference ($\Delta\phi$), path difference (Δx), wavelength (λ), speed of light (c) and frequency (f) are related as $\Delta\phi = 2\pi \Delta x/\lambda$ and $c = \lambda f$. During our measurements, we recorded the Tx-Rx distance (d) for each pair of Tx-Rx combinations, which we use as the path difference. Combining the above mentioned equations, the phase delay function is then defined as:

$$\phi_d(f) = (2\pi \ d \ f)/c. \qquad (4)$$

The Tx-Rx propagation delay is compensated by the phase delay function, $\phi_d(f)$, hence the phase information appears right from the line-of-sight (LoS)/ strongest arrival path instant. The real-valued part is obtained as the cosine component of the CTF magnitude:

$$\mathrm{Re}\{\tilde{H}(f)\}) = |H(f)| \ \cos\{\phi_d(f)\}. \qquad (5)$$

This real-valued part is then fed as the argument of the hilbert operator:

$$\hat{H}(f) = \mathcal{H}[\mathrm{Re}\{\tilde{H}(f)\}], \qquad (6)$$

that generates the complex-valued CTF, $\hat{H}(f)$. After applying the IFFT [48] on it, the corresponding PDP realization is obtained.

B. VALIDATION AND COMPARISON

To prove the validity/ accuracy of our method, we take advantage of the previous measurement campaign [29] in which 60 GHz intra-vehicular channel sounding was carried out in a sedan car employing a VNA. The phase data is first
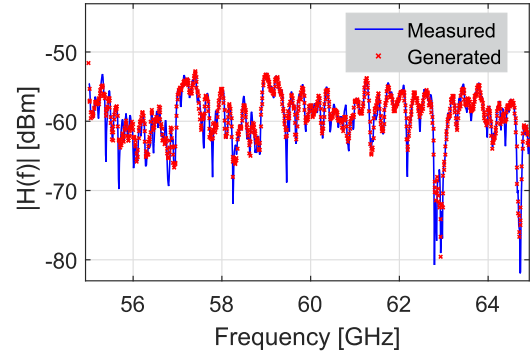

FIGURE 4. CTF amplitude measured and generated [car data].
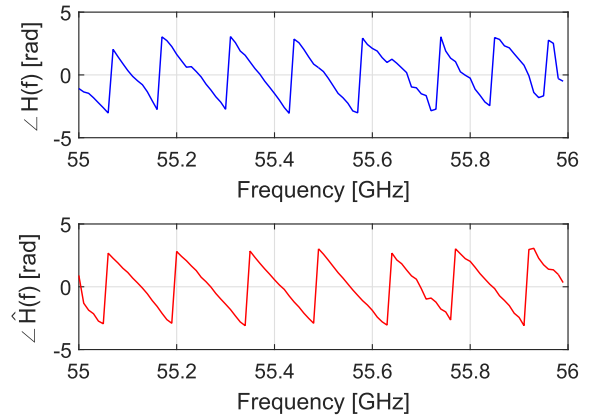

FIGURE 5. CTF phase measured and generated [car data].

removed from the recorded measurements and then we try to regenerate the complex-valued CTF, $\hat{H}(f)$, following the method proposed in the previous subsection.

Figs. 4 and 5 show the retrieved amplitude and phase plots, respectively, corresponding to a specific Rx-Tx position. This procedure is performed for all the data sets corresponding to the various Rx-Tx settings. The results have exhibited excellent agreement between both the estimated amplitude and phase plots and the true measurement data.

Next, IFFT is applied to the regenerated complex-valued CTFs which are then utilized to produce the PDPs. This is then compared with the PDPs produced directly by applying the IFFT on the VNA recorded data. Fig. 6 presents the PDP plots for four exemplary Tx-Rx settings. The generated PDPs closely resemble the corresponding measured PDP trails.

Table 1 summarizes the goodness-of-fit (GoF) results that gauge the similarity between the generated and the measured values of the PDP. We have considered three GoF metrics, correlation coefficient, root mean square error (RMSE) and Kolmogorov-Smirnov (K-S) test statistic. The correlation coefficient ($\hat{\rho}$) has been modeled according to [49]:

$$\hat{\rho} = \left| \frac{\frac{1}{N}\sum_{n=1}^{N}|P(n)||P_g(n)|}{\sqrt{\frac{1}{N}\sum_{n=1}^{N}|P(n)|^2 \frac{1}{N}\sum_{n=1}^{N}|P_g(n)|^2}} \right|, \qquad (7)$$

where $P(n)$ and $P_g(n)$ denote the data points for measured and generated PDPs, both of length N. Furthermore, the RMSE
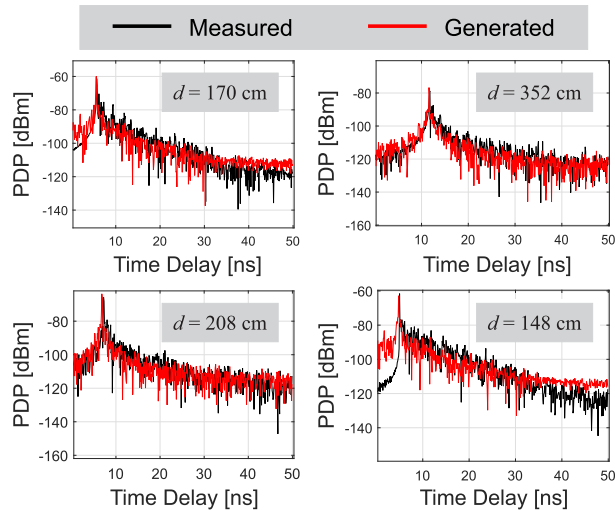
FIGURE 6. PDPs measured and generated [car data].

TABLE 1. GoF between measured and generated PDPs.

d [cm]	Correlation coefficient	RMSE ($\times 10^{-5}$)	K-S test statistics
72	0.7431	6.05	0.312
112	0.7240	2.54	0.122
119	0.6439	2.29	0.106
148	0.7844	6.48	0.175
149	0.8272	1.49	0.226
162	0.6681	3.29	0.245
165	0.7417	6.01	0.168
208	0.7485	6.27	0.170
352	0.6999	1.02	0.099

has been evaluated as [50]

$$\text{RMSE} = \sqrt{\frac{1}{N} \sum_{n=1}^{N} (|P(n)| - |P_g(n)|)^2}, \quad (8)$$

and the two-sample K-S test has been evaluated according to [51]

$$K = \max[F(|P(n)|) - F(|P_g(n)|)], \quad (9)$$

where K denotes the statistic test of the K-S test and F is the cumulative distribution function (CDF). The high values of the correlation coefficients demonstrate the existence of a strong association between the generated and the measured data. Low values of the RMSE between the two datasets and the two-sample K-S test statistic calculated with a 5% significance level corroborates the claim.

The efficacy of the proposed method is further proven as the time dispersion parameters are also estimated, i.e, the mean delay time ($\bar{\tau}$) and the root mean square (RMS) delay spread (τ_{rms}). These are the first moment and the second central moment of the PDP, respectively, and they are defined as [52]

$$\bar{\tau} = \frac{\sum_{\tau=0}^{\tau_{\max}} \tau P(\tau)}{\sum_{\tau=0}^{\tau_{\max}} P(\tau)}, \quad \text{and} \quad (10)$$

TABLE 2. Measured and generated time-delay parameters.

d [cm]	RMS delay spread [ns]		Mean delay time [ns]	
	Measured	Generated	Measured	Generated
72	9.38	9.38	19.54	19.42
112	9.04	9.02	20.05	19.96
119	8.96	8.93	20.12	20.01
148	8.66	8.62	20.66	20.46
149	8.63	8.60	20.69	20.83
162	8.51	8.50	20.80	20.73
165	8.47	8.49	20.96	20.85
208	8.01	8.01	21.44	21.33
352	6.67	6.66	23.68	23.64

$$\tau_{rms} = \sqrt{\frac{\sum_{\tau=0}^{\tau_{\max}} (\tau - \bar{\tau})^2 P(\tau)}{\sum_{\tau=0}^{\tau_{\max}} P(\tau)}}, \quad (11)$$

where $P(\tau) = \mathcal{E}\{|h(\tau)|^2\}$ is the received power at time-delay τ, i.e., the PDP; $\mathcal{E}\{\cdot\}$ is the expectation operator and τ is a discrete-time vector defined at the nonzero values of the CIR ($h(\tau)$), varying between 0 and a maximum time-delay ($\tau_{\max}$). Table 2 affirms our proposed approach by comparing the time dispersion parameters, $\bar{\tau}$ and τ_{rms}, of the measured and generated data sets.

Finally, the supremacy of our proposed approach is established as we analyze the same data with the approach proposed in [46], in which a blind Hilbert approach has been considered which is available in any commercial mathematical software package such as MATLAB. It does not exploit the Tx-Rx distance information available in the measurement data set. Fig. 7 shows the generated PDP and CTF from the method in [46], proving that applying basic HT can yield inaccurate results.
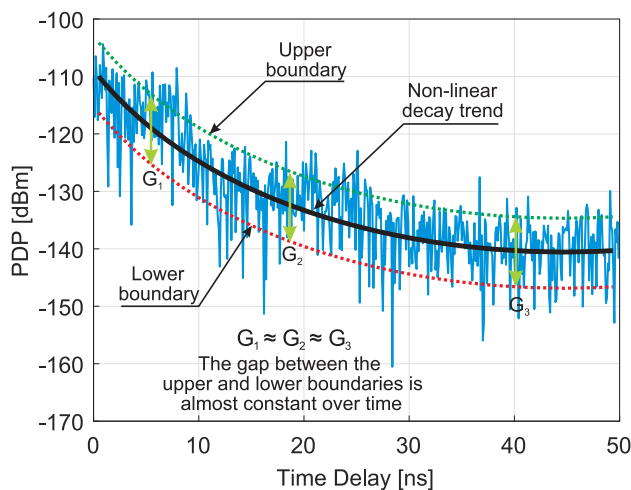
IV. PDP MODELLING AND SIMULATION

The propagation environment inside a bus is different from the conventional indoor scenarios, and often this can be attributed to the general construction of the interior of the bus. It was shown in [40] that although a higher value of path loss (PL) is expected at mmWave frequencies, it is possible to reach even the back seats of the bus with a single AP antenna mounted on the top of the driver seat at the front side of the bus. The reason behind this was the low value of PL coefficient, which was close to the free-space case, and this fact may be attributed to the metallic body of the bus which behaved as a waveguide and facilitated the wave propagation. The right side of a long distance commuter bus also have a different construction compared to the left side, with doors, staircases, place for toilet/ WC and a TV screen. This caused an additional PL of 2-3 dB. However, the effect of upholstery or curtains was not very significant.

As far as the small scale fading characteristics are concerned, the interior of the bus shows some typical characteristics as well. Fig. 8 shows a typical PDP inside the bus, where we summarize the general PDP trends as analyzed across all the experimental data sets. A statistical and visual examination of the measured PDP data reveals the following features:

(a) PDP

(b) CTF
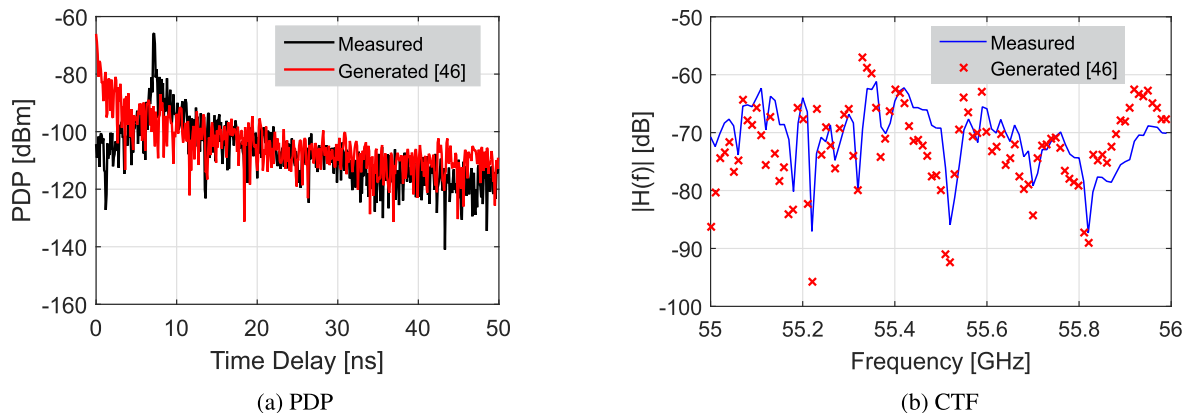
FIGURE 7. Generated PDP and CTF using the method proposed in [46]. The same car data is used to obtain the figures. Comparison of Fig. 7b with Fig. 4 and Fig. 7a with Fig. 6 shows that basic HT can give inaccurate results while the proposed modified HT gives accurate results.

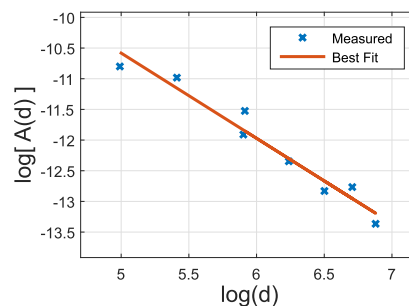**FIGURE 8.** General PDP trends inside the bus.

FIGURE 9. $\log(A(d))$ versus $\log(d)$ regression plot.

both the functions, i.e. $A(d) = \alpha d^m$ and $B(\tau) = \beta d^n$, which describes $f_d(\tau)$ as

$$f_d(\tau) = \alpha d^m \exp(\beta d^n \tau). \qquad (13)$$

The empirical values of $\log(A(d))$ with $\log(d)$ are plotted across several experiments in Fig. 9. Consequently, the values $m = -1.3891$ and $\alpha = -5.434 \times 10^{-2}$ are obtained from the line of best-fit.

From (13) we can write

$$\log_e \left[f_d(\tau)/(\alpha d^m) \right]/\tau = \beta d^n. \qquad (14)$$

From the regression plot in Fig. 9, it is possible to obtain the values for α and m. Next, with the help of (14), we can find the maximum likelihood values of β and n in a similar manner for all experiments (the corresponding fittings are omitted for brevity). After analyzing and calibrating the values of β and n across all the measured experimental data sets, we set them to $n = -0.4$ and $\beta = -1 \times 10^{-12}$.

Next, we define an adjustable boundary function, $b(\tau)$, to account for the variations between the upper and the lower bounds,

$$b(\tau) = \left(1 + \rho \log \left| \frac{\tau}{\tau_{scale}} + 1 \right| \right) f_d(\tau), \qquad (15)$$

where ρ and τ_{scale} govern the rate of decay of the small-scale PDP variation in (15) and are set to $\rho = 0.09$ and $\tau_{scale} = 10$.

1) When viewed in log scale, the PDPs decay in a nonlinear manner.
2) Again, in the log scale, the gross decay slope across the PDPs are quite close for identical d values.
3) There exists a power law relationship between the peak amplitude, say, $A(d)$, and d, across the PDPs. In the log-log scale, this is reflected as a linear decrease of the peak amplitude with distance.
4) The PDP values oscillate between a lower bound and an upper bound. The interval between the two boundaries does not change significantly with time delay.

A. ANALYTICAL PDP MODEL

From these observations, we may assume a PDP function of the form

$$f_d(\tau) = A(d) \exp[B(d) \, \tau], \qquad (12)$$

where, as defined earlier, $A(d)$ is the peak amplitude while $B(d)$ denotes the decay rate, and both are functions of d. A visual inspection inspires us to set power-law relation for

This boundary function helps us define the upper limit (b_U) and the lower limit (b_L) of the PDP as

$$b_U(\tau) = (1 - B/100 + \varepsilon)b(\tau), \qquad (16)$$

and

$$b_L(\tau) = (1 + \varepsilon)b(\tau), \qquad (17)$$

where B is the range of the PDP values expressed in dBm units and ε lowers the PDP curve by 100ε dBm. The following set of values, $\varepsilon = 0.005$, $B = 10$, was found to be optimum.

The simulated PDP, $P_s(\tau)$, for every time delay τ, can be finally obtained by generating a uniformly distributed random number,

$$P_s(\tau) = \mathcal{U}(b_L(\tau), b_U(\tau)), \qquad (18)$$

where, $\mathcal{U}(\cdot, \cdot)$ returns a uniform random number ranging between its arguments.

B. SIMULATION OF PDP
The method of generating PDP, which is discussed in Section IV-A in detail, is summed up in this subsection in the form of a pseudocode (see Algorithm 1). Our simulation algorithm takes Tx-Rx distance (d) as input and returns simulated channel PDP ($P_s(\tau)$) as output. The algorithm produces a continuous-time PDP starting from zero to a maximum time delay τ_{max} with a sampling rate $\tau_{res} = 1/\text{BW}$. Considering the dimensions of the bus, the parameter τ_{max} is set to 50 ns.

Algorithm 1 Channel PDP Simulation

Input: d [Tx-Rx distance]
Assignments: [Parameters]
    $\alpha \leftarrow -5.434 \times 10^{-2}$; $\beta \leftarrow -1 \times 10^{-12}$; $m \leftarrow -1.3891$;
    $n \leftarrow -0.4$; $B \leftarrow 10$; $\rho \leftarrow 0.09$; $\varepsilon \leftarrow 0.005$;
    $\tau \leftarrow 0$; $\tau_{scale} \leftarrow 10$; $\tau_{res} \leftarrow 10^{-10}$; $\tau_{max} \leftarrow 50 \times 10^{-9}$
1: **while** $\tau \leq \tau_{max}$ **do**
2:    $f_d(\tau) := \alpha d^m \exp(\beta d^n \tau)$
3:    $b(\tau) := \left(1 + \rho \log\left|\frac{\tau}{\tau_{scale}} + 1\right|\right) f_d(\tau)$
4:    $b_U(\tau) := (1 - B/100 + \varepsilon)b(\tau)$
5:    $b_L(\tau) := (1 + \varepsilon)b(\tau)$
6:    $P_s(\tau) := \mathcal{U}(b_L(\tau), b_U(\tau))$
7:    $\tau := \tau + \tau_{res}$
8: **end while**
Output: $P_s(\tau)$ [Simulated channel PDP]

A sample simulated PDP is shown in Fig. 10 along with the PDP obtained from the measurement data. The generated and measured PDPs compare pretty well with a strong correlation, the coefficient being greater than 0.7.

C. VALIDATION OF THE SIMULATION METHOD
To assess the performance of the simulation model, the same set of GoF tests are employed as done in Section III-B, with replacing $P_g(n)$ with $P_s(n)$, where $P_s(n)$ denote the data points for simulated PDPs. The values correlation coefficient, RMS error and K-S test are enlisted for 9 cases in Table 3.
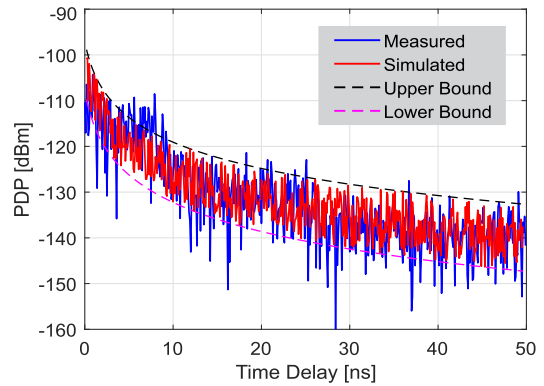

FIGURE 10. Simulated PDP [$d = 972$ cm, $\hat{\rho} = 0.7230$].

TABLE 3. GoF between measured and simulated PDPs.

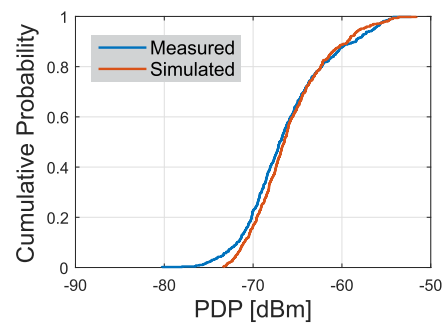| Expt. No.	d [cm]	Correlation coefficient	RMSE ($\times 10^{-5}$)	K-S test statistics
1	224	0.74	4.16	0.2072
2	366	0.71	2.48	0.2837
3	370	0.78	2.43	0.3924
4	512	0.71	1.38	0.2052
5	516	0.71	2.22	0.2334
6	666	0.72	0.96	0.1694
7	818	0.63	1.86	0.1855
8	970	0.71	2.11	0.2051
9	972	0.73	2.11	0.1515

FIGURE 11. CDFs of both measured and simulated PDPs.

The comparison is performed for all the measured test points, and PDPs calculated from the measured CTFs are compared to the corresponding PDPs simulated with the measured d value. In order to validate the proposed intravehicle channel model simulation, we have visualized the CDFs from the two-sample K-S test shown in Fig. 11 for a typical measurement scenario with a Tx-Rx separation of 5.16 m.

Finally, in Fig. 12 we show a comparison of the time dispersion parameters for the measured and the generated data sets using a comparative bar graph, showing how closely the simulated channel time dispersion parameters resemble the measured channel parameters across all the 9 experimental data sets.

V. BER PERFORMANCE ANALYSIS
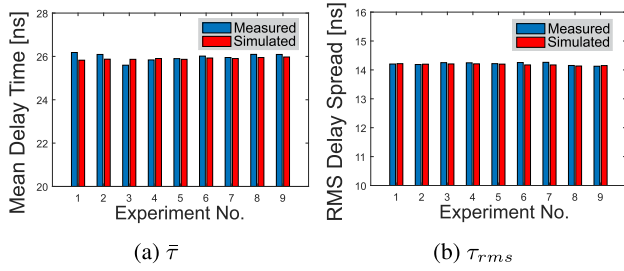A direct application of the proposed PDP simulation algorithm is the performance evaluation of the mmWave link in

FIGURE 12. Measured and simulated time-delay parameters.

FIGURE 13. Sample TDL realization [$d = 3.70$ m].

terms of the bit error rate (BER), which requires to discretize the PDP and derive an equivalent TDL model.

A. TDL MODEL

In a multipath fading wireless channel, if there exists a small number of distinctive multipath components (MPCs) or if the multipath components can be grouped into clusters where the path delays between clusters can be resolved but the MPC delays within a cluster are non-resolvable, then the channel can be modeled in the time-domain as a tapped-delay-line (TDL) filter. In the TDL model, delays between taps differentiate one scatterer group from the other and each tap represents the contribution of an individual scatterer group. The impulse response for the channel in this case can be conveniently expressed in the form [53]

$$h(t, \tau) = \sum_{i=0}^{N-1} \mathcal{G}_i \gamma_i(t) \delta(\tau - \tau_i), \qquad (19)$$

where N is the total number of taps, and $\mathcal{G}_i$, $\gamma_i(t)$ and τ_i are the gain, small-scale fading and delay of the $(i + 1)$th tap, respectively.

For our model we considered a uniform delay of $\tau_{i+1} - \tau_i = 5$ ns between taps and for a $\tau_{max} = 50$ ns,[2] the TDL model consisted of $N = 10$ taps. The first tap is normalized ($\mathcal{G}_0 = 0$ dB, $\gamma_0 = 1$), denoting the LoS/ strongest path, whereas the remaining tap gains are derived by sampling the simulated PDP and the small-scale fading coefficients following a Rayleigh process, $\gamma_i \sim \mathcal{CN}(0, 1)$, where $\mathcal{CN}(\mu, \sigma^2)$ denotes circularly symmetric complex-valued Gaussian random variable with mean μ and variance σ^2. Fig. 13 shows a typical channel realization obtained following our TDL model.

In Table 4, we enlist the tap gains obtained from the simulated PDPs for all the taps and for four different Tx-Rx separations. The distance values are chosen to represent different sections of the bus; a d value of 1.66 m (2.35 m) denotes the second (third) row from the front, the distance is 5.76 m to the seat near the middle door, and in the back seat d goes up to 9.72 m. As one can notice, the tap gains decay

TABLE 4. Tap gain for different d values.

Time Delay [ns]	Tap Gain [dB]			
	$d = 9.72$ m	$d = 5.76$ m	$d = 2.35$ m	$d = 1.66$ m
0	0	0	0	0
5	-5.3194	-6.9169	-7.9487	-7.3000
10	-7.7207	-8.9518	-12.8829	-11.8827
15	-12.3353	-11.6395	-15.5692	-14.8585
20	-12.5178	-13.9658	-17.1089	-16.8476
25	-13.6629	-15.1017	-18.9473	-19.2039
30	-16.0504	-16.9714	-20.9403	-20.5763
35	-16.6040	-16.8642	-22.8020	-21.8189
40	-17.3183	-17.2766	-24.3661	-23.0914
45	-17.2621	-18.3500	-24.7964	-24.0350
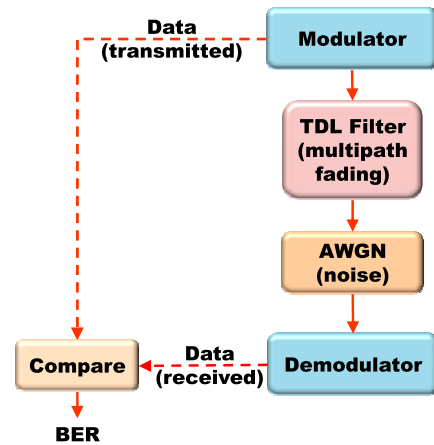
FIGURE 14. Block diagram for BER simulation.

sharply at the front rows, whereas at the back seat, the tap gain remains constant for the last four to five taps. The slow decrease of the tap gain indicates that the effect of multipath will be much more prominent at the back seats.

B. SIMULATION OF BER

The TDL model derived in the previous subsection is utilized to simulate the bit error rate performance. A general Monte Carlo simulation approach is followed and equivalent baseband modulation is employed to speed up the simulation. The BER simulations were performed in MATLAB and the block diagram for the BER evaluation is shown in Fig. 14.

---

[2]PDP record of 50 ns ensured that propagation paths having a path length of up to 15 m with multiple bounces inside the bus are taken into account. The differential delay of 5 ns symbolizes a data rate of 200 Mbit/s which can be changed by resampling of the PDP to obtain a TDL model having a different delay gap.
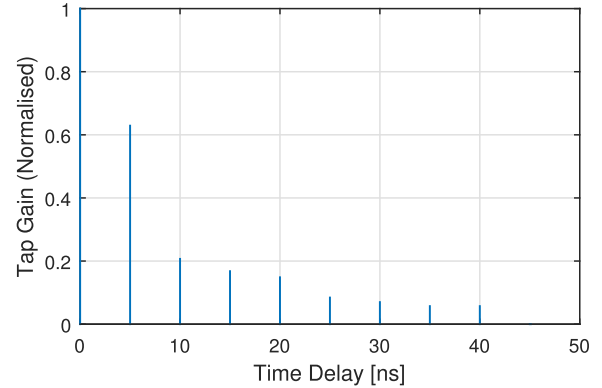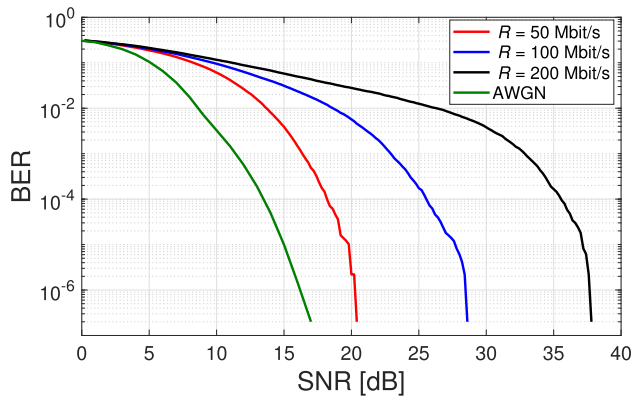
FIGURE 15. BER curves for different data rates.

During the simulation, a bit-stream of $B_N = 10^6$ data bits[3] were transmitted through the channel after modulation. The modulated signal is defined as

$$x(t) = \sum_{k=0}^{B_N} \hat{x}(k)\delta(t - k\tau_p), \qquad (20)$$

where τ_p is the sampling period of the input which, assuming a simple binary phase shift keying (BPSK) modulation, i.e. $\hat{x}(k) \in \{+1, -1\}$, renders $R = 1/\tau_p$ to be the transmitted bit rate and $E_b = \mathcal{E}\{\hat{x}^2(k)\}\tau_p$ to be the energy transmitted per bit.

The modulated signal is fed as the input to the multipath fading channel. The tap coefficients for various distances are taken from Table 4. The received signal is, $y(t) = x(t) * h(t) + n(t)$, where $*$ denotes the convolution operator and $n(t)$ is additive Gaussian white noise (AWGN) with double-sided power spectral density $N_0/2$. The output $y(t)$ is truncated from $t = 0$ to $t = B_N\tau_p$ and demodulated to recover the input signal. The demodulated bit-stream, $\hat{y}(t)$, is deduced as

$$\hat{y}(k) = \text{sign}\{y(t - k\tau_p)\}, \qquad (21)$$

and is compared to $\hat{x}(k)$. The number of mismatches are divided by B_N to compute the BER. During the simulations, BER is determined as a function of the signal-to-noise ratio (SNR), E_b/N_0.

Fig. 15 shows the BER variation with different data rates for a fixed d value of 1.66 m. BER curves are shown for three different data rates, 50 Mbit/s, 100 Mbit/s and 200 Mbit/s. These data rates are comparable to data rates available with wired cable modem or 4G cellular LTE networks. Fig. 15 shows that the SNR requirement may go up by 10 dB when the required data rate doubles. For lower bit rates, the effect of inter-symbol interference is reduced, as the information bits are spaced out. The AWGN BER curve is also shown as a reference.

Next, we plot the BER curves for varying Tx-Rx distances in Fig. 16 keeping the bit rate fixed at 100 Mbit/s. As the distance increases, the multipath environment degrades the signal. In our case, the access point is placed in front, so the back seat passenger experiences an additional

[3]Each time an averaging over 10^3 runs were performed to test BER up to the range 10^{-7}.
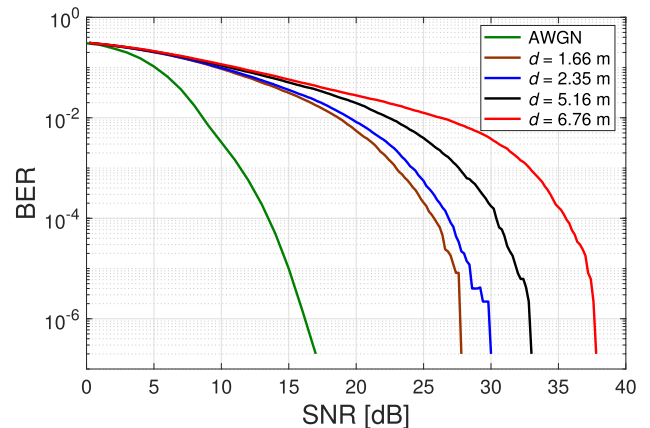

FIGURE 16. BER curves for different Tx-Rx distances.

SNR penalty of about only 10 dB compared to the front row passengers. This observation nullifies the myth that mmWave cannot propagate over larger distances in confined environments. The BER curves indicate that if a proper link margin is maintained, it is possible to use 60 GHz hardware to provide broadband access with desired reliability.

VI. CONCLUSION
The article presents measurement-based modeling and performance evaluation of 60 GHz mmWave wireless link inside a bus. Comprehensive measurements are conducted to study the PDP behavior which led to the development of an analytical framework followed by an algorithmic flowchart to simulate PDPs. Simulated PDP values are used to derive a TDL equivalent link model which forms the basis for link performance evaluation. It is observed that the distance of the user from the access point and the specified data rate has a large impact on the BER performance of the intravehicular mmWave link. Although the modeling and analysis is carried out for a bus, the characterization is applicable for other public transport vehicles (e.g. subway coaches, trams and trolleybuses) which have similar internal structures and comparable dimensions.

REFERENCES
[1] J. Kim, H. Chung, G. Noh, S. W. Choi, I. Kim, and Y. Han, "Overview of moving network system for 5G vehicular communications," in *Proc. IEEE EuCAP*, Apr. 2019, pp. 1–5.

[2] M. Andersson, N. Lavesson, and T. Niedomysl, "Rural to urban long-distance commuting in Sweden: Trends, characteristics and pathways," *J. Rural Stud.*, vol. 59, pp. 67–77, Apr. 2018.

[3] A. Künn-Nelen, "Does commuting affect health?" *Health Econ.*, vol. 25, no. 8, pp. 984–1004, Aug. 2016.

[4] S. Vincent-Geslin and E. Ravalet, "Determinants of extreme commuting. Evidence from Brussels, Geneva and Lyon," *J. Transp. Geography*, vol. 54, pp. 240–247, Jun. 2016.

[5] E. Costa-Montenegro, F. Quinoy-Garcia, F. J. Gonzalez-castano, and F. Gil-Castineira, "Vehicular entertainment systems: Mobile application enhancement in networked infrastructures," *IEEE Veh. Technol. Mag.*, vol. 7, no. 3, pp. 73–79, Sep. 2012.

[6] M. Nieuwenhuijsen, J. Bastiaanssen, S. Sersli, E. O. D. Waygood, and H. Khreis, "Implementing car-free cities: Rationale, requirements, barriers and facilitators," in *Proc. Integrating Hum. Health Urban Transp. Planning*, Jul. 2018, pp. 199–219.

[7] M. J. Nieuwenhuijsen and H. Khreis, "Car free cities: Pathway to healthy urban living," *Environ. Int.*, vol. 94, pp. 251–262, Sep. 2016.

[8] C. Calastri, S. Borghesi, and G. Fagiolo, "How do people choose their commuting mode? An evolutionary approach to travel choices," *Economia Politica*, vol. 13, pp. 1–26, Feb. 2018.

[9] A. Lieberoth, N. H. Jensen, and T. Bredahl, "Selective psychological effects of nudging, gamification and rational information in converting commuters from cars to buses: A controlled field experiment," *Transp. Res. Part F, Traffic Psychol. Behav.*, vol. 55, pp. 246–261, May 2018.

[10] N. Hoang-Tung, A. Kojima, and H. Kubota, "Impacts of travellers' social awareness on the intention of bus usage," *IATSS Res.*, vol. 39, no. 2, pp. 130–137, Mar. 2016.

[11] T. A. Myrvoll, J. E. Håkegård, T. Matsui, and F. Septier, "Counting public transport passenger using WiFi signatures of mobile devices," in *Proc. IEEE 20th Int. Conf. Intell. Transp. Syst. (ITSC)*, Oct. 2017, pp. 1–6.

[12] S. Maaroufi and S. Pierre, "Vehicular social systems: An overview and a performance case study," in *Proc. ACM DIVANet*, Montreal, QC, Canada, Sep. 2014, pp. 17–24.

[13] M. Xiao, S. Mumtaz, Y. Huang, L. Dai, Y. Li, M. Matthaiou, G. K. Karagiannidis, E. Björnson, K. Yang, I. Chih-Lin, and A. Ghosh, "Millimeter wave communications for future mobile networks," *IEEE J. Sel. Areas Commun.*, vol. 35, no. 9, pp. 1909–1935, Sep. 2017.

[14] A. Al-Dulaimi, X. Wang, and I. Chih-Lin, *5G Networks: Fundamental Requirements, Enabling Technologies, and Operations Management*. Hoboken, NJ, USA: Wiley, 2018.

[15] K. David and H. Berndt, "6G vision and requirements: Is there any need for beyond 5G?" *IEEE Veh. Technol. Mag.*, vol. 13, no. 3, pp. 72–80, Sep. 2018.

[16] L. Kong, M. K. Khan, F. Wu, G. Chen, and P. Zeng, "Millimeter-wave wireless communications for IoT-cloud supported autonomous vehicles: Overview, design, and challenges," *IEEE Commun. Mag.*, vol. 55, no. 1, pp. 62–68, Jan. 2017.

[17] I. Mavromatis, A. Tassi, R. J. Piechocki, and A. Nix, "Efficient millimeter-wave infrastructure placement for city-scale ITS," Mar. 2019, *arXiv:1903.01372*. [Online]. Available: https://arxiv.org/abs/1903.01372

[18] Y. Ghasempour, C. R. C. M. D. Silva, C. Cordeiro, and E. W. Knightly, "IEEE 802.11 ay: Next-generation 60 GHz communication for 100 Gb/s Wi-Fi," *IEEE Commun. Mag.*, vol. 55, no. 12, pp. 186–192, Dec. 2017.

[19] A. Bamba, F. Mani, and R. D'Errico, "Millimeter-wave indoor channel characteristics in V and E bands," *IEEE Trans. Antennas Propag.*, vol. 66, no. 10, pp. 5409–5424, Oct. 2018.

[20] A. W. Mbugua, K. Saito, F. Zhang, and W. Fan, "Characterization of human body shadowing in measured millimeter-wave indoor channels," in *Proc. IEEE 29th Annu. Int. Symp. Pers., Indoor Mobile Radio Commun. (PIMRC)*, Bologna, Italy, Sep. 2018, pp. 1–5.

[21] S. Li, Y. Liu, L. Lin, D. Sun, S. Yang, and X. Sun, "Simulation and modeling of millimeter-wave channel at 60 GHz in indoor environment for 5G wireless communication system," in *Proc. IEEE Int. Conf. Comput. Electromag. (ICCEM)*, Mar. 2018, pp. 1–3.

[22] A. F. Molisch, A. Karttunen, R. Wang, C. U. Bas, S. S. Korea, S. S. Korea, and J. Zhang, "Millimeter-wave channels in urban environments," in *Proc. 10th Eur. Conf. Antennas Propag. (EuCAP)*, Apr. 2016, pp. 1–5.

[23] W. Schafer and E. Lutz, "Propagation characteristics of short-range radio links at 60 GHz for mobile intervehicle communication," in *Proc. SBT/IEEE Int. Symp. Telecommun.*, Rio de Janeiro, Brazil, Sep. 1990, pp. 212–216.

[24] D. L. Didascalou, F. Kuchen, and W. Wiesbeck, "An investigation of millimeter wave propagation mechanisms for mobile intervehicle communications and outdoor MBS," in *Proc. 48th IEEE Veh. Technol. Conf. Pathway Global Wireless Revolution*, May 1998, pp. 1800–1804.

[25] A. Kato, K. Sato, M. Fujise, and S. Kawakami, "Propagation characteristics of 60-GHz millimeter waves for ITS inter-vehicle communications," *IEICE Trans. Commun.*, vol. 84, no. 9, pp. 2530–2539, Sep. 2001.

[26] H. Sawada, T. Tomatsu, G. Ozaki, H. Nakase, S. Kato, K. Sato, and H. Harada, "A sixty GHz intra-car multi-media communications system," in *Proc. IEEE 69th Veh. Technol. Conf.*, Apr. 2009, pp. 1–5.

[27] K. Fujita, H. Sawada, and S. Kato, "Intra-car communications system using radio hose," in *Proc. IEEE Asia–Pacific Microw. Conf.*, Dec. 2010, pp. 57–60.

[28] R. Nakamura and A. Kajiwara, "Empirical study on 60GHz in-vehicle radio channel," in *Proc. IEEE Radio Wireless Symp.*, Jan. 2012, pp. 327–330.

[29] A. Chandra, P. Kukolev, T. Mikulášek, and A. Prokeš, "Frequency-domain in-vehicle channel modelling in mmW band," in *Proc. IEEE 1st Int. Forum Res. Technol. Soc. Ind. Leveraging Better Tomorrow (RTSI)*, Sep. 2015, pp. 106–110.

[30] M. Peter, W. Keusgen, A. Kortke, and M. Schirrmacher, "Measurement and analysis of the 60 GHz in-vehicular broadband radio channel," in *Proc. IEEE 66th Veh. Technol. Conf.*, Sep. 2007, pp. 834–838.

[31] R. Felbecker, W. Keusgen, and M. Peter, "Ray-tracing simulations of the 60 GHz incabin radio channel," in *Proc. URSI GASS*, Aug. 2008, pp. 1–4.

[32] M. Schack, M. Jacob, and T. Kürner, "Comparison of in-car UWB and 60 GHz channel measurements," in *Proc. IEEE 4th Eur. Conf. Antennas Propag.*, Apr. 2010, pp. 1–5.

[33] J. Blumenstein, A. Prokes, A. Chandra, T. Mikulasek, R. Marsalek, T. Zemen, and C. Mecklenbräuker, "In-vehicle channel measurement, characterization and spatial consistency comparison of 3-11 GHz and 55-65 GHz frequency bands," *IEEE Trans. Veh. Technol.*, vol. 66, no. 5, pp. 3526–3537, May 2017.

[34] A. Prokes, T. Mikulasek, J. Blumenstein, C. F. Mecklenbrauker, and T. Zemen, "Intra-vehicle ranging in ultra-wide and millimeter wave bands," in *Proc. IEEE Asia–Pacific Conf. Wireless Mobile (APWiMob)*, Aug. 2015, pp. 246–250.

[35] L. Azpilicueta, P. L. Iturri, E. Aguirre, J. J. Astrain, J. Villadangos, C. Zubiri, and F. Falcone, "Characterization of wireless channel impact on wireless sensor network performance in public transportation buses," *IEEE Trans. Intell. Transp. Syst.*, vol. 16, no. 6, pp. 3280–3293, Dec. 2015.

[36] H. Suzuki, Z. Chen, and I. B. Collings, "Analysis of practical MIMO-OFDM performance inside a bus based on measured channels at 5.24 GHz," in *Proc. IEEE 2nd Eur. Conf. Antennas Propag. EuCAP*, Nov. 2007, pp. 1–8.

[37] D. W. Matolak and A. Chandrasekaran, "5 GHz intra-vehicle channel characterization," in *Proc. IEEE Veh. Technol. Conf.*, Sep. 2012, pp. 1–5.

[38] B. Li, C. Zhao, H. Zhang, X. Sun, and Z. Zhou, "Characterization on clustered propagations of UWB sensors in vehicle cabin: Measurement, modeling and evaluation," *IEEE Sensors J.*, vol. 13, no. 4, pp. 1288–1300, Apr. 2013.

[39] V. Semkin, A. Ponomarenko-Timofeev, A. Karttunen, O. Galinina, S. Andreev, and Y. Koucheryavy, "Path loss characterization for intra-vehicle wearable deployments at 60 GHz," Jan. 2019, *arXiv:1902.01949*. [Online]. Available: https://arxiv.org/abs/1902.01949

[40] A. Chandra, T. Mikulasek, J. Blumenstein, and A. Prokes, "60 GHz mmW channel measurements inside a bus," in *Proc. IEEE 8th IFIP Int. Conf. Technol., Mobility Secur.*, Larnaca, Cyprus, Nov. 2016, pp. 1–5.

[41] A. U. Rahman, U. Ghosh, A. Chandra, and A. Prokes, "Channel modelling for 60GHz mmWave communication inside bus," in *Proc. IEEE Veh. Netw. Conf. (VNC)*, Taipei, Taiwan, Dec. 2018, pp. 1–6.

[42] I. Karls and M. Mueck, "V2X requirements, standards, and regulations," in *Networking Vehicles to Everything: Evolving Automotive Solutions*. Berlin, Germany: De Gruyter, 2018, ch. 3, pp. 59–88.

[43] E. Uhlemann, "Continued dispute on preferred vehicle-to-vehicle technologies," *IEEE Veh. Technol. Mag.*, vol. 12, no. 3, pp. 17–20, Sep. 2017.

[44] K. Sjoberg, P. Andres, T. Buburuzan, and A. Brakemeier, "Cooperative intelligent transport systems in Europe: Current deployment status and outlook," *IEEE Veh. Technol. Mag.*, vol. 12, no. 2, pp. 89–97, Jun. 2017.

[45] B. P. Donaldson, M. Fattouche, and R. W. Donaldson, "Characterization of in-building UHF wireless radio communication channels using spectral energy measurements," *IEEE Trans. Antennas Propag.*, vol. 44, no. 1, pp. 80–86, Jan. 1996.

[46] A. Prokes, T. Mikulasek, J. Blumenstein, and J. Vychodil, "Usability of Hilbert transform for complex channel transfer function calculation in 60 GHz band," in *Proc. PIERS*, Nov. 2017, pp. 2945–2951.

[47] M. Kyrö, S. Ranvier, V. M. Kolmonen, K. Haneda, and P. Vainikainen, "Long range wideband channel measurements at 81-86 GHz frequency range," in *Proc. IEEE 4th Eur. Conf. Antennas Propag. EuCAP*, Barcelona, Spain, Apr. 2010, pp. 1–5.

[48] T. Domínguez-Bolaño, J. Rodríguez-Piñeiro, J. A. García-Naya, and L. Castedo, "Experimental characterization of LTE wireless links in high-speed trains," *Wireless Commun. Mobile Comput.*, vol. 2017, pp. 1–20, Sep. 2017.

[49] M. S. Sharawi, A. T. Hassan, and M. U. Khan, "Correlation coefficient calculations for MIMO antenna systems: A comparative study," *Int. J. Microw. Wireless Technol.*, vol. 9, no. 10, pp. 1991–2004, Dec. 2017.

[50] R. J. Hyndman and A. B. Koehler, "Another look at measures of forecast accuracy," *Int. J. Forecasting*, vol. 22, no. 4, pp. 679–688, Oct. 2006.

[51] F. J. Massey, Jr., "The Kolmogorov-Smirnov test for goodness of fit," *J. Amer. Statist. Assoc.*, vol. 46, no. 3, pp. 68–78, 1951.

[52] A. J. Goldsmith, *Wireless Communications*. Cambridge, U.K.: Univ. Press, 2005.

[53] T. Blazek, M. Ashury, C. F. Mecklenbräuker, D. Smely, and G. Ghiaasi, "Vehicular channel models: A system level performance analysis of tapped delay line models," in *Proc. IEEE 15th Int. Conf. ITS Telecommun. (ITST)*, Warsaw, Poland, May 2017, pp. 1–8.

ANIRUDDHA CHANDRA (M'08–SM'16) received the B.E., M.E., and Ph.D. degrees from Jadavpur University, Kolkata, India, in 2003, 2005, and 2011, respectively. He joined the Electronics and Communication Engineering Department, National Institute of Technology, Durgapur, India, in 2005, where he is currently an Associate Professor. In 2011, he was a Visiting Lecturer with the Asian Institute of Technology, Bangkok. From 2014 to 2016, he was a Marie Curie Fellow with the Brno University of Technology, Czech Republic. He has published about 80 research papers in refereed journals and peer-reviewed conferences. His research interest includes physical layer issues in wireless communication. He was a co-recipient of the Best Short Paper Award at the IEEE VNC 2014, Paderborn, Germany, and delivered a keynote lecture at the IEEE MNCApps 2012, Bengaluru, India.

ANIQ UR RAHMAN (S'18) is currently pursuing the B.Tech. degree with the Department of Electronics and Communication Engineering, National Institute of Technology, Durgapur (NITD), India, where he also serves as the Chair of the IEEE Student Branch. He was a Summer Intern with the European Organization for Nuclear Research (CERN), Switzerland, in 2018. He is also an Avid Programmer and an Open Source Enthusiast and was accepted in the Google Summer of Code Program, in 2017, where he was a Software Developer Intern with Robocomp, Universidad de Extremadura, Spain, in 2017. His research interests include wireless communication, signal processing, and the Internet of Things.

USHASI GHOSH (S'18) is currently pursuing the degree with the Department of Electronics and Communication Engineering, National Institute of Technology, Durgapur, India. She was a Summer Research Intern with the IIT Kanpur, Kanpur, India, in 2018. Prior to that, she was also a Research Intern with the IIT Hyderabad, India. Her research interest includes the broad area of wireless communications.

JOSÉ A. GARCÍA-NAYA (S'07–M'10) received the M.Sc. and Ph.D. degrees in computer engineering from the University of A Coruña (UDC), A Coruña, Spain, in 2005 and 2010, respectively, where he has been with the Group of Electronics Technology and Communications, since 2005, and is currently an Associate Professor. He is the coauthor of more than 90 peer-reviewed papers in journals and conferences. His research interests include the experimental evaluation of wireless systems in realistic scenarios (indoors, outdoors, high mobility, and railway transportation), signal processing for wireless communications, wireless sensor networks, specially devoted to indoor positioning systems, and time-modulated antenna arrays applied to wireless communication systems. He is also a member of the research team of more than 40 research projects funded by public organizations and private companies.

ALEŠ PROKEŠ received the M.Sc., Ph.D., and Habilitation degrees from the Brno University of Technology (BUT), in 1988, 1999, and 2006, respectively, where he has been with the Faculty of Electrical Engineering and Communication, since 1990, and is currently a Professor. Since 2013, he has been the Head of the Research Center of Sensor, Information and Communication Systems, and Radio-Frequency Systems Group. He has coauthored 30 journal publications and more than 40 conference papers. His research interests include measurement and modeling of channels for V2X communication, optimization, and design of optical receivers and transmitters for free-space optics (FSO) systems, influence of atmospheric effects on optical signal propagation, evaluation of FSO availability and reliability, higher order non-uniform sampling and signal reconstruction, and software-defined radio.

JIRI BLUMENSTEIN (M'17) received the Ph.D. degree from the Brno University of Technology, in 2013. In 2011, he was a Researcher with the Institute of Telecommunications, TU Wien. He has cooperated with several companies, including Racom, Volkswagen, and ON Semiconductor, in the areas of applied research of wireless systems and fundamental research funded by the Czech Science Foundation. He is currently a Researcher with the Department of Radio Electronics, Brno University of Technology. His research interests include signal processing, physical layer of communication systems, channel characterization and modeling, and wireless system design.

CHRISTOPH F. MECKLENBRÄUKER (S'88–M'97–SM'08) received the Dipl.Ing. degree (Hons.) in electrical engineering from TU Wien, in 1992, and the Dr.Ing. degree (Hons.) from the Ruhr-Universität Bochum, Bochum, Germany, in 1998. From 1997 to 2000, he was with Siemens AG, Austria, where he was engaged in the standardization of the radio access network for UMTS. From 2000 to 2006, he was a Senior Researcher with the Telecommunications Research Center Vienna (FTW), Vienna. In 2006, he joined the Institute of Communications and Radio Frequency Engineering, TU Wien, as a Full Professor. From 2009 to 2016, he led the Christian Doppler Laboratory for Wireless Technologies for Sustainable Mobility. He has authored approximately 250 papers in international journals and conferences, for which he has also served as a Reviewer. He holds several patents in the field of mobile cellular networks. His current research interests include radio interfaces for peer-to-peer networks (vehicular connectivity and sensor networks), ultra-wideband radio, and MIMO transceivers. He is also a member of the Antennas and Propagation Society, the Intelligent Transportation Society, the Vehicular Technology Society, the Signal Processing Society, VDE, and EURASIP. He is also the Councilor of the IEEE Student Branch Wien. His doctoral dissertation received the Gert-Massenberg Prize, in 1998.